Carbohydrate Polymers 94 (2013) 773–781

Contents lists available at SciVerse ScienceDirect

Carbohydrate Polymers

journal homepage: www.elsevier.com/locate/carbpol

Characterization of cellulose II nanoparticles regenerated from 1-butyl-3-methylimidazolium chloride

Jingquan Han[a], Chengjun Zhou[a], Alfred D. French[b], Guangping Han[c], Qinglin Wu[a,*]

[a] School of Renewable Natural Resources, Louisiana State University AgCenter, Baton Rouge, LA 70803, United States
[b] USDA ARS, 1100 Robert Lee Boulevard, New Orleans, LA 70124, United States
[c] Material Science and Engineering College, Northeast Forestry University, Harbin 150040, China

ARTICLE INFO

Article history:
Received 17 September 2012
Received in revised form 11 January 2013
Accepted 4 February 2013
Available online 13 February 2013

Keywords:
Ionic liquid
Crystal structure
Microcrystalline cellulose
Cotton
Regeneration
Dissolution

ABSTRACT

Regenerated cellulose nanoparticles (RCNs) including both elongated fiber and spherical structures were prepared from microcrystalline cellulose (MCC) and cotton using 1-butyl-3-methylimidazolium chloride followed by high-pressure homogenization. The crystalline structure of RCNs was cellulose II in contrast to the cellulose I form of the starting materials. Also, the RCNs have decreased crystallinity and crystallite size. The elongated RCNs produced from cotton and MCC had average lengths of 123 ± 34 and 112 ± 42 nm, and mean widths of 12 ± 5 and 12 ± 3 nm, respectively. The average diameter of spherical RCNs from MCC was 118 ± 32 nm. The dimensions of the various RCNs were all well fitted with an asymmetrical log-normal distribution function. The RCN has a two-step pyrolysis, different from raw MCC and cotton that have a one-step process.

1. Introduction

Cellulose, a linear polysaccharide composed of β-1–4-linked D-glucopyranose repeating units, exhibits a number of desirable properties and has become one of the most promising renewable polymeric materials. Besides the application of unmodified cellulose products, cellulose can be converted into regenerated cellulosic materials, which have been widely applied in many fields (Jiang et al., 2012; Mahmoudian, Wahit, Ismail, & Yussuf, 2012). However, due to its partly crystalline structure, closely packed chains with van der Waals interactions, and numerous inter- and intra-molecular hydrogen bonds, cellulose cannot be dissolved in water or most conventional organic solvents. This poses a formidable obstacle to increased utilization of cellulose. Therefore, it is essential to further explore suitable cellulose dissolution methods to expedite novel applications of regenerated cellulose (Jiang et al., 2012; Lan, Liu, Yue, Sun, & Kennedy, 2011; Mahmoudian et al., 2012).

A limited number of solvent systems have been investigated for cellulose dissolution and regeneration. These include N-methylmorpholine-N-oxide (NMMO) (Zhao et al., 2007), N-dimethylacetamide/lithium chloride (DMAC/LiCl) (Zhang, Liu, Zheng, & Zhu, 2012), dimethyl sulfoxide/paraformaldehyde (DMSO/PF) (Jiang et al., 2012), 1,3-dimethyl-2-imidazolidinone/lithium chloride (DMI/LiCl) (Tamai, Tatsumi, & Matsumoto, 2004), and NaOH/Urea solution (Kuo & Lee, 2009). Among the solvents mentioned above, only the NMMO/water system is currently commercialized for manufacturing regenerated cellulose products, leading to the man-made cellulose with the generic name, Lyocell (Jiang et al., 2012). However, this solvent has some disadvantages associated with its application, including volatility, toxicity, formation of byproducts, demand for harsh conditions, difficulty of solvent recovery, process instability, requirement of activation before dissolution, and investment in safety technology (Lan et al., 2011; Mahmoudian et al., 2012).

Recently, a new type of solvent, ionic liquids (ILs), has been gaining interest because of their potential to be eco-friendly. They have characteristics such as low melting point, low flammability, non-volatility, non-explosiveness, thermal stability and ease of recycling, and thus can possibly replace conventional volatile organic solvents (Gutowski et al., 2003; Mahmoudian et al., 2012). Structurally, ILs are composed of ions, but exist as liquids at relatively low temperatures (usually lower than 100 °C). Rogers et al. (Swatloski, Spear, Holbrey, & Rogers, 2002) first showed that ILs could be nonderivatizing solvents for cellulose, and that cellulose could be dissolved in ILs without any pretreatment. So far, ILs have shown great potential for cellulose processing (Li et al., 2009) because they are efficient solvents for biomass that allow

* Corresponding author. Tel.: +1 225 578 8369; fax: +1 225 578 4251.
E-mail addresses: qwu@agcenter.lsu.edu, wuqing@lsu.edu (Q. Wu).

0144-8617/$ – see front matter © 2013 Elsevier Ltd. All rights reserved.
http://dx.doi.org/10.1016/j.carbpol.2013.02.003

easy regeneration of cellulose upon anti-solvent addition. Compared to the NMMO/water system, dissolving cellulose in ILs is safer and easier, and the ILs can be recovered and reused after the cellulose regeneration by methods such as evaporation, ionic exchange, reverse osmosis, and salting out (Gutowski et al., 2003). By evaporating the anti-solvents, the recovery rate of $[BMIM]^+[Cl]^-$ can exceed 99.5% (Gutowski et al., 2003; Quan, Kang, & Chin, 2010). For these reasons, ILs could replace organic solvents for a wide range of applications. Zhang and coworkers (2007) demonstrated that regenerated cellulose exhibited good mechanical properties. The dissolution and regeneration of cellulose with ILs can promote the utilization of cellulosic materials by combining two main green chemistry principles: using environmentally preferable solvents and bio-renewable feed-stocks (Zhu et al., 2006). Dissolution in ILs has the potential to become a crucial pretreatment for enhancing enzymatic hydrolysis of cellulose because it can be done under mild condition (Kuo & Lee, 2009).

The desirable properties of ILs can be tailored by judicious variation of the chemical structures of the cation and/or the anion of the ILs (Azubuike, Rodriguez, Okhamafe, & Rogers, 2012). The most common IL for cellulose dissolution is 1-butyl-3-methylimidazolium chloride ($[BMIM]^+[Cl]^-$), producing a cellulose solution without derivation (Lan et al., 2011; Swatloski et al., 2002). As is always found with dissolution and regeneration of cellulose (Mansikkamäki, Lahtinen, & Rissanen, 2007; Zhao et al., 2007), the crystal structure of cellulose that is dissolved in $[BMIM]^+[Cl]^-$ takes the usual cellulose II allomorph upon regeneration (Quan et al., 2010). ILs provide for versatile modification of the properties of cellulose II powders (Azubuike et al., 2012). Besides applications in smart materials, such as electro-activepaper (EAPap), sensors and actuators, regenerated cellulose II products have some preferable properties over cellulose I powders. Uses such as the recently introduced new filler/binder for solid dosage forms, and have been recommended as a second-generation multifunctional direct compression excipient, affording the manufacture of rapidly disintegrating tablets (Azubuike et al., 2012; Kumar, de la Luz Reus-Medina, & Yang, 2002). Hence, the fundamental research needs to be conducted in order to characterize in detail the cellulose II products regenerated from ILs.

In the present work, the process of dissolving and regenerating cotton and MCC cellulose using $[BMIM]^+[Cl]^-$ was studied. Regeneration was conducted by an anti-solvent strategy. The properties of regenerated cellulose II nanoparticles from MCC and cotton were evaluated and compared. The objective of this study was to characterize the morphology, crystal structure, functional groups and thermal properties of the regenerated cellulose nanoparticles prepared with $[BMIM]^+[Cl]^-$.

2. Materials and methods

2.1. Materials

An IL, 1-butyl-3-methylimidazolium chloride ($[BMIM]^+[Cl]^-$) with a melting point of 70 °C and a molecular weight of 174.67, was purchased from Sigma-Aldrich (St. Louis, MO). Cotton fabric was first cut into 4 × 20-mm fragments using a fabric cutter and then ground into smaller particles with a Wiley mill (Arthur H. Thomas Corp., Philadelphia, PA) to pass through an 80-mesh screen. The obtained particles were washed with ethanol and distilled water to remove impurities and then dried overnight in a vacuum oven (EQ-DZF-6020, MTI Corp.) at 60 °C. Microcrystalline cellulose (MCC) (Avicel FD-100 MCC, FMC Biopolymer, Philadelphia, PA) was dried overnight in a vacuum oven at 60 °C before use. Acetone, ethanol and deionized water were purchased from Sigma–Aldrich (St. Louis, MO) and used without further processing. All the reagents and solvents used were of analytical grade.

2.2. Preparation of cellulose nanoparticles

2.2.1. Dissolution process

Before use, solid state $[BMIM]^+[Cl]^-$, cotton and MCC were vacuum-dried at 70 °C for 12 h to remove the remnants of water. The presence of water can significantly impair cellulose solubility in IL by competing with the IL for hydrogen bonds to the cellulose microfibrils (Swatloski et al., 2002). After the $[BMIM]^+[Cl]^-$ totally melted into liquid, the dried MCC or cotton samples (5%, w/w) were slowly added into $[BMIM]^+[Cl]^-$ liquid with vigorous stirring. The heterogeneous mixture was immediately transferred into reaction vials. The vials were sealed and then heated in a silicone-oil bath at 125 °C for a period of 5 h. The dissolution process was carried out on a magnetic hot plate stirrer with safety control (Ret control, VISC., IKAMAG, CHEMGLASS-1990-35). The reaction temperature was controlled by a PT-100 temperature sensor (PFA coated), which was directly inserted into the silicone-oil. The viscosity of the 5% (w/w) cellulose/$[BMIM]^+[Cl]^-$ solution appeared to decrease with reaction temperature and time. Therefore, in order to achieve an optimum stirring effect, the stirring velocity of the magnetic stir bar (PTFE) in each reaction vial was kept at 150 rpm during the first 2 h, and subsequently was kept constant at 350 rpm during the following 3 h. After the 5 h incubation period, a light amber-colored, translucent and viscous solution was formed, indicating the termination of the reaction between cellulose samples and $[BMIM]^+[Cl]^-$.

2.2.2. Regeneration process

Distilled water was applied as the anti-solvent to stop the reaction and regenerate the cellulose nanoparticles from $[BMIM]^+[Cl]^-$. After the dissolution process, the cellulose/$[BMIM]^+[Cl]^-$ suspension was poured into an excess of distilled water and off-white precipitates formed immediately. After being stirred for about 20 min, the precipitates temporarily dispersed in the solution. The diluted suspension was filtered through filter paper (Grade-5, Whatman) under vacuum. The powdery off-white solids were then filtered and washed repeatedly with ethanol and water/acetone mixture. Subsequently, the filtered products were re-dispersed in distilled water and then centrifuged at 40 °C for 20 min with a constant speed of 12,000 rpm (Sorvall RC-5B Refrigerated Superspeed Centrifuge, Du Pont Instruments) to further remove the residual $[BMIM]^+[Cl]^-$. Thereafter, the precipitates, which were centrifuged three times, were eventually placed in regenerated cellulose dialysis tubes (Fisher Scientific, Pittsburgh, PA, USA) with a molecular weight cut off of 12,000–14,000 and dialyzed against distilled water for 24 h. After a series of filtering, centrifugation, and dialysis operations, hydrophilic $[BMIM]^+[Cl]^-$ was eliminated from the final product. The final concentration of the cellulose aqueous suspension was about 1% (w/w). The suspensions were stored at 10 °C. Based on the initial weight of the cellulose in $[BMIM]^+[Cl]^-$, the yield of the reconstituted cellulose II nanoparticles was estimated to be 30–40 wt.%. The RCNs prepared from MCC and cotton were designated as M-RCNs and C-RCNs, respectively.

2.2.3. Homogenization process

To further enhance the dispersion of RCNs in water, mechanical homogenization was applied to the RCN suspension. The RCNs in aqueous suspension was processed through a high-pressure homogenizer (Microfluidizer M-110P, Microfluidics Corp., Newton, MA, USA) equipped with a pair of Z-shaped interaction chambers (one 200 μm ceramic, and one 87 μm diamond) under an operating pressure of 207 MPa (Yue et al., 2012). After ten passes through the homogenizer, the final RCN suspensions lacked visible aggregation and presented a pale bluish–purple color, indicating an excellent dispersity of nanoparticles in aqueous suspension. The homogenized M-RCNs and C-RCNs suspensions were stored at 10 °C.

2.2.4. Freeze-drying process

The M-RCN and C-RCN suspensions were frozen by mixing acetone and dry ice in an ice pot. The samples were immediately dried by using a freeze-dryer (FreeZone, 2.5 plus, Labconco Corp., Kansas City, MO, USA) for 2 days. The final freeze-dried M-RCNs and C-RCNs were stored in plastic bags before performing further characterizations.

2.3. Characterization

2.3.1. Wide-angle X-ray diffraction (WXRD)

It is well known that the mechanical properties of cellulose products were strongly dependent on the crystallinity and crystal structure. To determine the crystal structure and crystallinity, WXRD patterns of the untreated MCC, raw cotton, M-RCNs and C-RCNs were measured by Bruker/Siemens D5000X-ray automated powder X-ray diffractometer. Before testing, cotton and MCC powder samples were dried in a vacuum oven at 60 °C for 24 h to remove moisture. The M-RCN and C-RCN powder samples were obtained by freeze drying their corresponding suspensions. The WXRD data were generated by a diffractometer with Cu-Ka radiation ($\lambda = 1.542$ Å) at 40 kV and 30 mA over the range $2\theta = 5°–40°$, a size step of 0.02°, and a time step of 2.0 s, (1.0 h per scan). The data were further analyzed using the MDI Jade 6.5.26 software (Serial#: MDI-R99691, Materials Data Inc., Livermore, CA). For each sample, the background was fitted with a software-generated cubic-spline function. Subsequently, the whole pattern was smoothed three times by a parabolic filter to reduce excess noise. The degree of crystallinity or crystallinity index (CI, %) for each sample was determined (Kumar, Mago, Balan, & Wyman, 2009; Li et al., 2010):

$$\mathrm{CI}(\%) = 100\frac{I_{\mathrm{Max}} - I_{\mathrm{Am}}}{I_{\mathrm{Max}}} \quad (1)$$

where I_{Max} is the maximum intensity of the principal peak, and I_{Am} is the intensity of diffraction attributed to amorphous cellulose.

The crystallite size of each sample perpendicular to the (2 0 0) planes, w (nm), was calculated by the Scherrer equation (Liu, Liu, Yao, & Wu, 2010):

$$w = \frac{K\lambda}{\beta \cos\theta} \quad (2)$$

where θ is the diffraction angle, $K = 0.94$ (correction factor), $\lambda = 0.154$ nm and β is the corrected angular width in radians at half maximum intensity of the [2 0 0] peak.

2.3.2. Fourier transform infrared spectrometry (FTIR)

FTIR spectra of raw cotton, untreated MCC, C-RCNs and M-RCNs were measured with a Bruker FTIR analyzer (Tensor-27, Bruker Optics Inc., Billerica, MA) in the attenuated total reflectance (ATR) mode. All spectra were obtained in transmittance mode on a Zn/Se ATR crystal cell at room temperature. For each measurement, approximately 5 mg of the freeze-dried powder samples were pressed into the sample chamber of FTIR equipment and then 64 scans were taken with a resolution of 4 cm^{-1} and a spectral range of 4000–600 cm^{-1}. Three replicated measurements were recorded for each condition.

2.3.3. Transmission electron microscopy (TEM)

For the analysis, the concentration of the aqueous RCN suspensions was diluted from 1% to 0.01% (w/w). The diluted RCN suspension was treated with an ultrasonic bath (Model 3510, Branson, MS) prior to the TEM operation. A droplet (5 μl) of a diluted suspension of RCNs was negatively stained with a droplet (5 μl) of 2% (wt) uranyl acetate for about 2 min to enhance the contrast of the TEM images. Then the mixture was immediately deposited on the surface of a 400-mesh carbon-coated copper grid. The excess liquid on the grid was absorbed by using a tiny piece of filter paper to touch the edge of the grid. The morphology of obtained RCNs was characterized by using TEM (JEOL 100CX, JEOL, Inc., Peabody, MA) with an accelerating voltage of 80 kV. The distribution of RCN dimensions was evaluated from TEM images by using ImageJ 1.45k software (Rasband, W.S., ImageJ, U. S. National Institutes of Health, Bethesda, MD, http://imagej.nih.gov/ij/, 1997–2011). For each sample, one hundred particles were randomly selected and measured from several TEM images. The statistics and histograms of RCN dimensions were calculated and designed by Origin 8.5.0 software (SR1 b161, OriginLab Corp., Northampton, MA).

2.3.4. Thermogravimetric analysis (TGA)

The degradation and dehydration of M-RCNs and C-RCNs were characterized by a thermo-gravimetric analyzer TGA (TA Q50 Instruments Inc., New Castle, DE) in a nitrogen atmosphere. Approximately 5 mg freeze-dried samples in a platinum pan were heated from 50 to 550 °C at a heating rate of 10 °C/min under a nitrogen flow of 60 mL min^{-1}. Before the data acquisition segment, the sample was equilibrated at 25.00 °C for 5 min to obtain an isothermal condition. The weight-loss rate was obtained from derivative thermogravimetric (DTG) data.

3. Results and discussion

3.1. WXRD analysis

The WXRD results showed that the regeneration of MCC and cotton resulted in significant changes in crystalline structure and crystallinity. The WXRD patterns of raw cotton and untreated MCC had a different structure compared to their corresponding regenerated cellulose nanoparticles produced by $[BMIM]^+[Cl]^-$ (Fig. 1). Fig. 1a shows that the WXRD pattern of native cotton sample had the three characteristic peaks of cellulose I crystal structure at $2\theta = 14.9°$, 16.4°, and 22.5° assigned to (1 $\bar{1}$ 0), (1 1 0), and (2 0 0), respectively. Upon dissolution and regeneration of cotton cellulose in the $[BMIM]^+[Cl]^-$ solvent system, the characteristic peaks were found at $2\theta = 11.7°$ (1 $\bar{1}$ 0), 20.1° (1 1 0), and 21.6° (0 2 0), which were attributed to the cellulose II crystalline allomorph. Nearly identical, cellulose I peaks were found for untreated MCC, and the same cellulose II peaks were found for regenerated MCC. This transformation from cellulose I to cellulose II because of dissolution and regeneration in $[BMIM]^+[Cl]^-$ agrees with earlier findings (Quan et al., 2010). Therefore, $[BMIM]^+[Cl]^-$ cannot only be used to extract cellulose nanoparticles from lignocellulosic biomass (as discussed below), but also help convert cellulose I to cellulose II during the process.

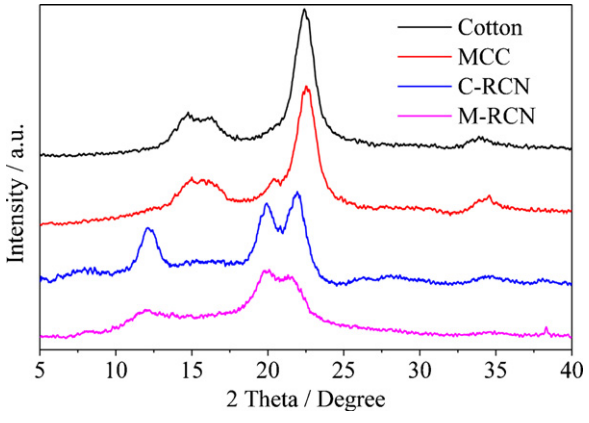

Fig. 1. X-ray diffraction analysis of raw cotton, C-RCNs, untreated MCC and M-RCNs.

The crystallinity index is related to the strength and stiffness of fibers (Wang, Han, et al., 2007; Wang, Ding, et al., 2007). After the dissolution and regeneration in $[BMIM]^+[Cl]^-$, the CI of the M-RCN and C-RCN were 52.1% and 61.8%, compared to the values of 76.7% and 80.0% for the native material, respectively. The similar decrease in CI values for reconstituted cellulose II powders was previously reported in the literatures. (Azubuike et al., 2012; Jin, Wang, Wang, & Zhao, 2012; Kumar et al., 2002). Note that CI values for cellulose I and II cannot be directly compared, but in general comparable crystallinities of I and II should result in substantially lower CI values for cellulose I. This is because the 16° 2-θ position for measuring the amorphous intensity for cellulose II is considerably further from neighboring peaks than is the 18° 2-θ position for cellulose I peaks (AD French and M Santiago Citrón, manuscript in preparation.) Therefore, in the present case, with CI values for the RCN being lower than the untreated cotton and MCC samples, the crystallinities of the RCN much would be much lower. Lower CI implied a more amorphous structure, resulting in a more disordered structure, which was also observed in TEM images below. Besides, the crystallite size of untreated MCC and cotton cellulose calculated perpendicular to the (2 0 0) planes were 54.6 and 56.9 nm, while the M-RCNs and C-RNCs had a crystallite size of 51.2 and 48.9 nm, respectively. The reduced crystallite sizes of RNCs were likely because of the incomplete growing of crystallites after regeneration (Gao, Shen, & Lu, 2011). It was reported that the regenerated celluloses with lower CI are much easier to be enzymatically hydrolyzed to glucose, providing a better pretreated cellulose source for biodegradation process (Lee, Doherty, Linhardt, & Dordick, 2009).

3.2. FTIR analysis

The original cotton powders and C-RCNs obtained after treatment with $[BMIM]^+[Cl]^-$ showed similar FTIR spectra (Fig. 2). For original cotton powders, the broad bands in the 3650–3000 cm^{-1} region were hydrogen-bond O—H stretching vibrations and the peak at 2900 cm^{-1} corresponded to -CH stretching vibrations (Lu & Hsieh, 2010). After $[BMIM]^+[Cl]^-$ treatment, the —CH stretching vibration was shifted from 2901 cm^{-1} to 2893 cm^{-1}, the CO at C-6 stretching vibration was moved from 1033 cm^{-1} to 1025 cm^{-1}, and

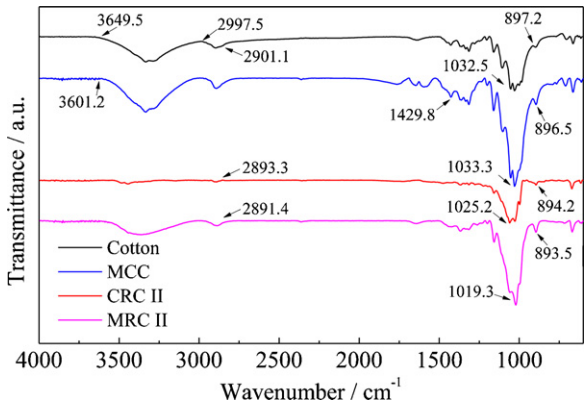

Fig. 2. FTIR spectra of raw cotton, C-RCNs, untreated MCC and M-RCNs.

COC vibration at β-glycosidic linkage was switched from 897 cm^{-1} to 894 cm^{-1} (Table 2). The transformation could be explained by changes in the torsion angles of the glycosidic linkge (Ray & Sarkar, 2001). These changes in the FTIR spectra of cotton cellulose upon reacting with $[BMIM]^+[Cl]^-$ indicated that $[BMIM]^+[Cl]^-$ transformed the cellulose crystal structure from I to II. The untreated MCC and M-RCNs obtained after treatment with $[BMIM]^+[Cl]^-$ showed similar FTIR spectra (Fig. 2). Both MCC and M-RCNs spectra showed strong hydrogen bonded —OH stretching vibrations in the range of 3600–3000 cm^{-1}. The $—CH_2—(C_6)—$ bending vibration and —CH stretching vibration had peaks around 1430 and 2900 cm^{-1}, respectively. The peak at 1644 cm^{-1} was the O—H bending of adsorbed water. Some typical band characteristics of FTIR spectra related to the transition from cellulose I to cellulose II were also observed in Table 1 Table 1. In addition, the absence of $[BMIM]^+[Cl]^-$ peaks in the spectra of M-RCNs and C-RCNs indicated that the IL was completely removed during the purification sequence of filtering, centrifugation, and dialysis. Therefore, the FTIR data together with the XRD results confirmed that the crystal structure was transformed from cellulose I to cellulose II during the IL treatments.

Table 1
Band characteristics of FTIR spectra related to transition from cellulose I–II.

Raw material	Peak assignment					
	—CH stretching (cm^{-1})		—CO at C-6 stretching (cm^{-1})		COC at β-glycosidic linkage (cm^{-1})	
	BT[a]	AT	BT	AT	BT	AT
Cotton	2901	2893	1033	1025	897	894
MCC	2900	2892	1033	1025	896	893

[a] BT and AT: before and after the $[BMIM]^+[Cl]^-$ treatment.

Table 2
The dimension statistics of M-RCNs, C-RCNs and spherical RCNs (S-RCNs).

Parameters	C-RCNs		M-RCNs		S- RCNs
	Length (nm)	Width (nm)	Length (nm)	Width (nm)	Diameter (nm)
Sample size	100	100	100	100	100
Mean	123	12	112	12	118
Maximum	197	23	204	23	226
Mode (M)	125	13	113	13	107
Minimum	60	4	39	6	47
Standard deviation (S)	34	5	42	3	32
95% CI of mean[a]	[116,130]	[12,13]	[103,120]	[11,13]	[112,125]
Aspect ratio[b]	9.96	9.21	NA		

[a] 95% Confidence interval.
[b] Aspect ratio is calculated by mean of length divided by mean of width.

3.3. Morphology and dimension distribution of regenerated cellulose II nanoparticles

Fig. 3 shows the typical TEM micrographs of M-RCNs and C-RCNs. Fig. 3a and b shows that M-RCNs and C-RCNs present similar shape and moderate dispersibility. They were wavy, disordered and partly fused, which might be caused by the reduced crystallinity of cellulose (confirmed by WXRD patterns). Similar morphology was also observed in the regenerated cellulose II fibers by the TEMPO-mediated oxidation or alkaline treatments (Hirota, Tamura, Saito, & Isogai, 2012). In addition, some curve-structured nanoparticles appeared to form thicker bundles of aggregates for M-RCNs and C-RCNs that are slightly different from the needle-like cellulose nanocrystals/whiskers produced by conventional acid hydrolysis process (Liu et al., 2010). Similar observations were reported previously, and the cellulose in aqueous suspension is known to have a general tendency to aggregate in parallel with each other (Marchessault, Morehead, & Walter, 1959). Several possible explanations for cellulose aggregation were presented previously in related studies. The negative staining was considered to induce an artificial aggregation of cellulose on the surfaces of carbon-coated copper grids, because water and uranyl acetate were evaporated and blotted up in the drying step (Elazzouzi-Hafraoui et al., 2008). Another reason for agglomeration is a surface ionic charge of the cellulose (Liu et al., 2010).

To evaluate the dimension of M-RCNs and C-RCNs based on TEM observations, the nanoparticles in aqueous suspension needs to be further dispersed by high-pressure homogenization process. Compared with M-RCNs (Fig. 3a) and C-RCNs (Fig. 3b) without high-pressure homogenization, some homogenized M-RCNs (Fig. 3d) and C-RCNs (Fig. 3c) presented a relatively uniform shape, and partial RCN aggregates were separated to a certain degree. Occasional aggregation still existed after high-pressure homogenization. This phenomenon suggested that high-pressure homogenization treatment could partly disperse the aggregated cellulose by intense mechanical shearing forces and enhance the dispersibility of cellulose in aqueous suspension (Liu et al., 2010).

The dimension of homogenized M-RCNs and C-RCNs is presented in Table 2 Table 2 and the size distribution of each sample was plotted as histogram (Fig. 4). Because cellulose tended to agglomerate in parallel and overlap longitudinally, the accurate determination of RCN dimensions was challenging. It was believed that cellulose II had some disordered regions or defects at 100–200 nm intervals periodically present along the length

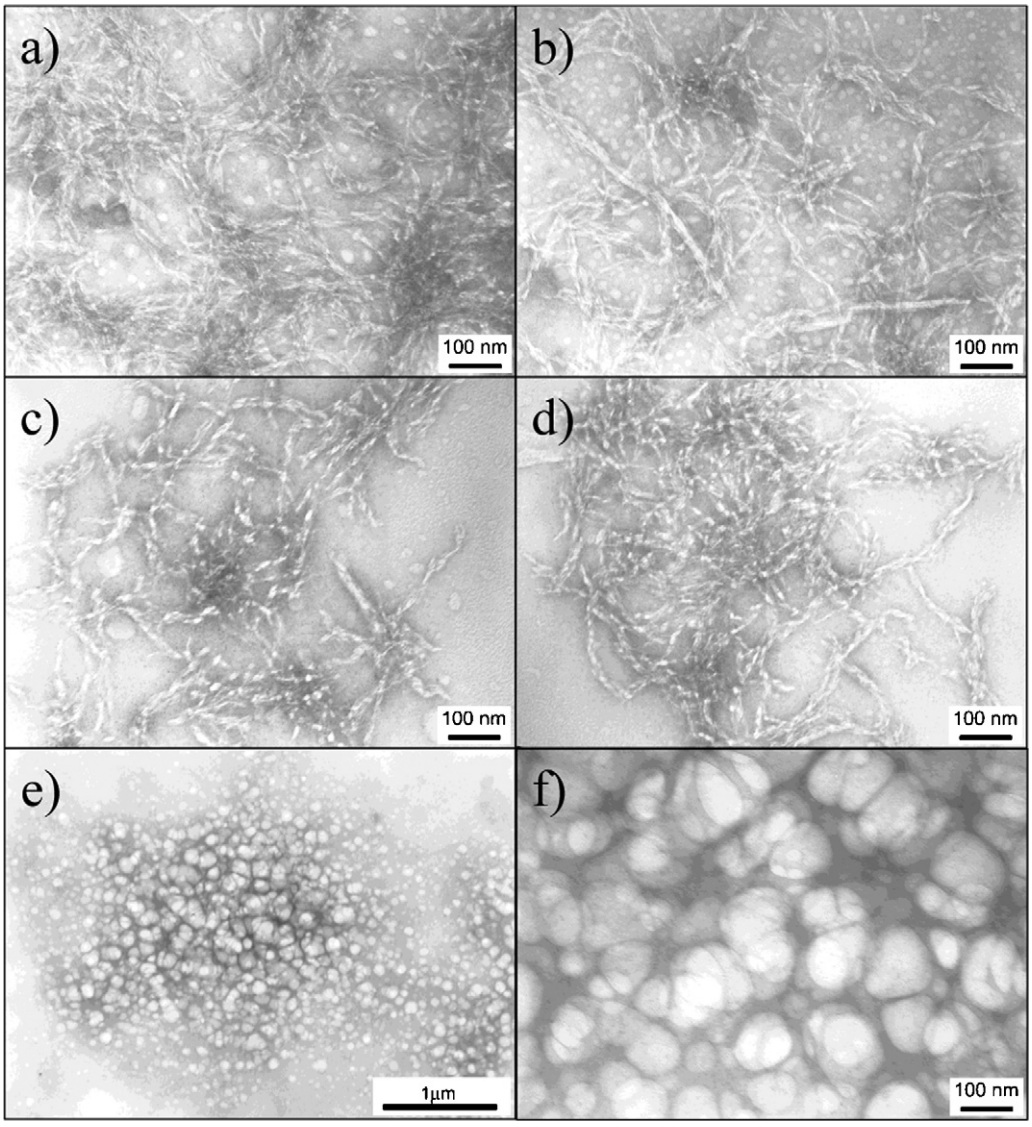

Fig. 3. TEM images of M-RCNs (a), C-RCNs (b), homogenized M-RCNs (c), homogenized C-RCNs (d) and spherical RCNs (e).

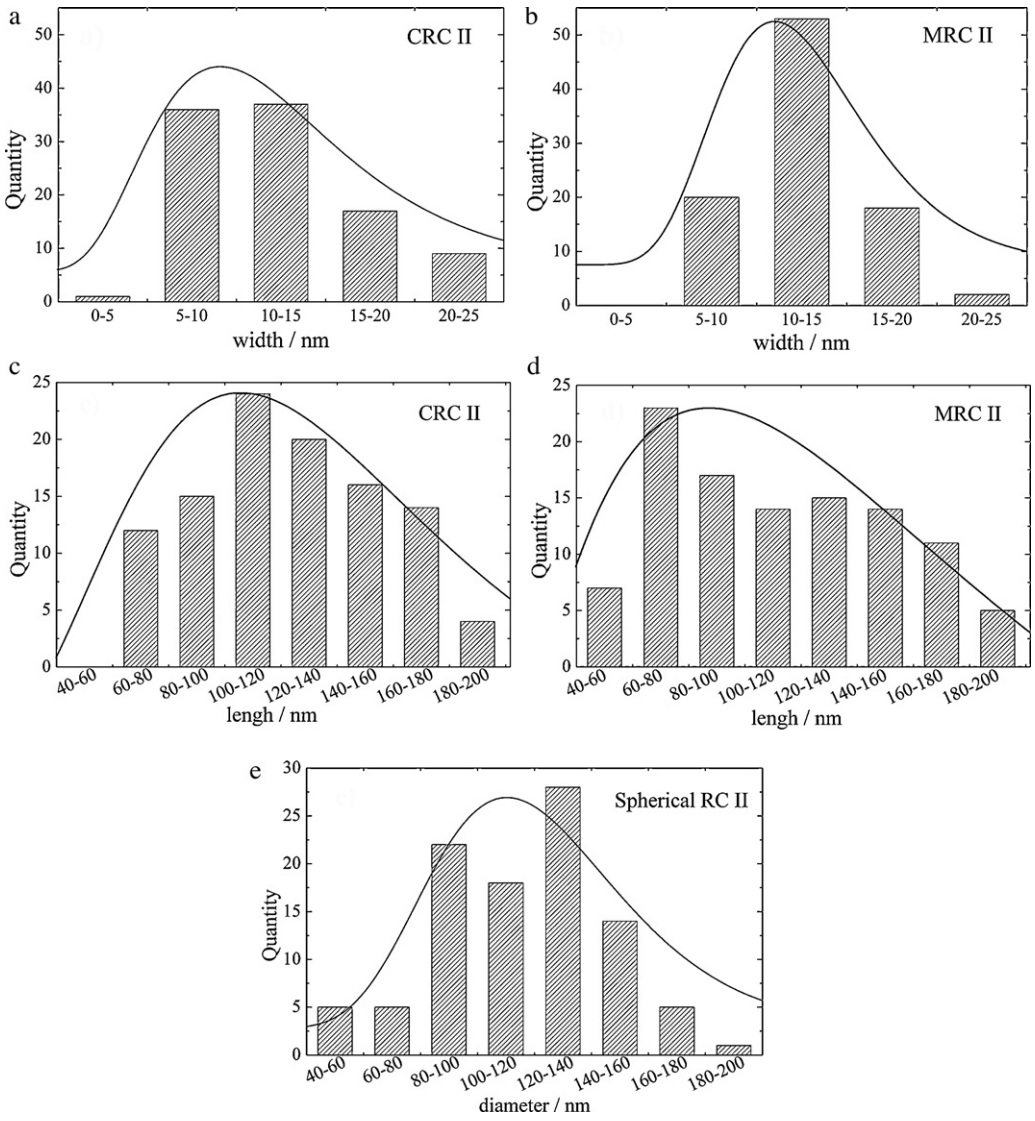

Fig. 4. The dimension distribution of homogenized M-RCNs, C-RCNs and spherical RCNs. (a) and (b) width distribution of C-RCNs and M-RCNs; (c) and (d) length distribution of C-RCNs and M-RCNs; (e) diameter distribution of spherical RCNs.

direction, which was defined as the dimension of cellulose II nanoparticles (Hirota et al., 2012). Therefore, the length and width of RCNs can be measured directly from TEM images by using ImageJ 1.45k software. The width was defined as the largest dimension measured along the each nanoparticle, perpendicular to its long axis (Elazzouzi-Hafraoui et al., 2008). The statistical results of RCN dimensions are summarized in Table 2. For fiber- type C-RCNs, the average width and length were approximately 12 ± 5 and 123 ± 34 nm, respectively. The corresponding aspect ratio was 9.96 calculated by mean length/mean width. For fiber- type M-RCNs, the mean width and length were approximately 12 ± 3 and 112 ± 42 nm, respectively. The dimension of RCNs was similar to that of the regenerated cellulose II nanoparticles prepared by TEMPO-mediated oxidation of mercerized cellulose (Hirota et al., 2012) The corresponding aspect ratio was 9.21, which is slightly less than the aspect ratio of C-RCNs. It was reported that these celluloses II nanoparticles regenerated from ILs had relatively better flow properties and higher bulk and tap densities, which was advantageous in tableting, especially in the manufacture of tablets with high-dose drugs (Azubuike et al., 2012).

The corresponding size distribution of M-RCNs and C-RCNs was further plotted on the histograms in Fig. 4. All the lengths and widths showed an asymmetrical log-normal distribution (referred to as a Galton's distribution). Previous studies applied a log-normal function Y to fit this type of size distribution of objects obtained by fragmentation (Elazzouzi-Hafraoui et al., 2008):

$$Y = Ke^{\frac{-(\ln M)^2 - \ln X}{S^2}} \quad (3)$$

where S is the standard deviation, K is the fitting coefficient, and M is the mode. To obtain the specific equations for each sample, the corresponding S and M values were statistically calculated using Origin 8.5 software and are summarized in Table 2.

In addition to the fiber-type nanoparticles, spherical regenerated cellulose II nanoparticles (Spherical RCNs) produced from MCC were also observed in TEM images (Fig. 3e and f). Fig. 1f with a 100 nm scale bar is an enlarged image of the central part of Fig. 1e with a 1 μm scale bar. The average diameter was 118 ± 32 nm (Table 2). The approximate spherical RCNs formed irregular aggregates from their initial globular particles. Similar spherical cellulose II particles were previously observed in the 12% (w/w) NaOH treated bacterial cellulose (Shibazaki, Kuga, & Okano, 1997). In addition, similar spherical cellulose I that resulted from a mild acid hydrolysis concentration, or from a combination of both

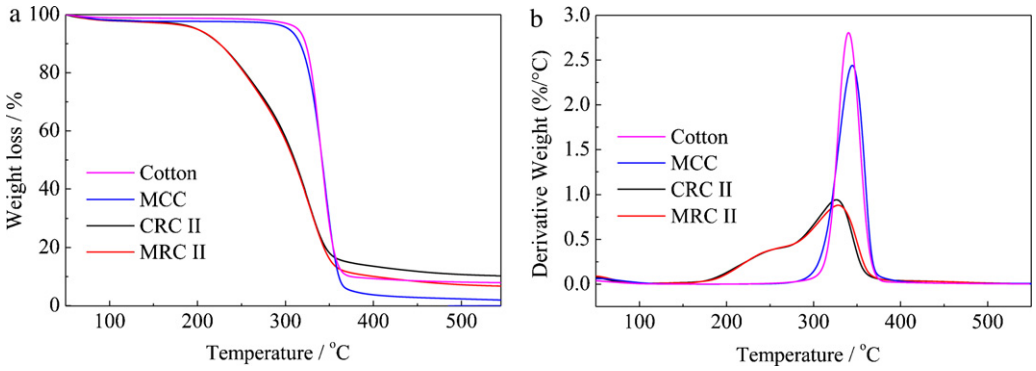

Fig. 5. Thermo gravimetric (TG) curves (a) and derivatives of thermo gravimetric (DTG) curves (b) for untreated MCC, M-RCNs, raw cotton, and C-RCNs.

hydrochloric and sulfuric acids and ultrasonic treatment have also been reported. The spherical cellulose demonstrated better thermal stability than fiber-like cellulose (Lu & Hsieh, 2010; Wang, Han, et al., 2007; Wang, Ding, et al., 2007; Wang, Ding, & Cheng, 2008). Since $[BMIM]^+[Cl]^-$ can dissolve cellulose more effectively than acid solutions at certain conditions, the formation mechanism of spherical RCNs in ILs could be inferred from the perspective of reaction kinetics. For acid hydrolysis of cellulose molecules, the hydrolysis reaction started from the surface and then gradually permeated into the inner amorphous region (Wang et al., 2008). In contrast, $[BMIM]^+[Cl]^-$, with a better capability of dissolving cellulose, the IL molecules could instantly penetrate the inner amorphous region of cellulose, leading to a simultaneous reaction both at the surface and in the inner amorphous regions of MCC. This process might cause some MCC particles to first transfer to the irregular spherical shape, instead of fiber-like cellulose nanoparticles.

3.4. TGA analysis

Thermo gravimetric (TG) curves and derivatives of thermo gravimetric (DTG) curves of raw cotton, untreated MCC and the corresponding freeze-dried M-RCNs and C-RCNs are shown in Fig. 5 Fig. 5. Table 3 Table 3 lists extrapolated onset temperature (T_o, °C), the maximum thermal degradation temperature (T_{max}, °C), the maximum weight loss rate (R_{max}, %/°C) and char yields (CY, %) for various samples. All samples had a small weight loss in the low temperature (less than 125 °C) range, corresponding to the evaporation of absorbed water in raw materials and final RCN materials.

The original MCC showed a typical decomposition behavior with an onset degradation temperature (T_0) of 300.3 °C, and the maximum thermal degradation temperature (T_{max}) occurred at 344.3 with the maximum weight loss rate (R_{max}) of 2.4%/°C (Table 3). The degradation of the original MCC occurred within a relatively narrow temperature range and had only one pyrolysis process in the DTG curve. The main mass loss step of the original MCC ranged from 300.3 to 376.1 °C. The corresponding char yield (CY) at 550 °C is 1.9%.

On the other hand, the M-RCNs showed a different decomposition behavior than the original MCC (Fig. 5 a). The more gradual thermal transitions began at a relatively lower T_0 of 205.8 °C. Similar gradual thermal transitions of cellulose were reported previously (Lu & Hsieh, 2010). The degradation of M-RCNs occurred within a wider temperature range and had two well-separated pyrolysis processes in the DTG curve. The first process of weight loss ranged from 205.8 °C to 268.2 °C with the T_{max} at 254.7 °C. The second, which dominated the overall pyrolysis, ranged from 268.2 °C to 361.4 °C with the T_{max} at 328.4 °C, having relatively higher char residue, nearly 6.7%, at 550 °C (Fig. 5b). A similar two-step pyrolysis of acid-treated cellulose nanocrystals was reported previously (Wang, Han, et al., 2007; Wang, Ding, et al., 2007).

For the original cotton (Fig. 5a), a typical decomposition trend with an onset degradation temperature of 310.6 °C was observed, and this coincided with a large mass loss, resulting in 7.9% char yield (CY) at 550 °C. The maximum thermal degradation temperature (T_{max}) occurred at 340.3 °C with the maximum weight loss rate (R_{max}) of 2.7%/°C (Table 3). The degradation of the original cotton occurred within a relatively narrow temperature range and had only one pyrolysis process in the DTG curve. The main mass loss step of the original cotton ranged from 310.6 to 368.7 °C.

Similarly, the C-RCNs also exhibited significantly different thermal behavior than the original cotton, showing more gradual thermal transitions that began at a relative lower T_0 of 200.8 °C. The degradation of C-RCNs occurred within a wider temperature range and had two well-separated pyrolysis processes in the DTG curve. The C-RCNs lost approximately 25% of the original mass in the 200.8–273.4 °C region followed by another 55% mass loss between 273.4 and 366.7 °C, having a relatively higher char residue, nearly 10.3% CY, at 550 °C. The maximum thermal degradation temperatures (T_{max}) of stage 1 and stage 2 were 258.7 °C and 325.8 °C, respectively, and the corresponding CY were 0.4 and 0.9%/°C, respectively (Fig. 5b).

Therefore, the untreated MCC and native cotton samples showed similar one-step pyrolysis processes, while the M-RCNs and C-RCNs had similar two-step pyrolysis processes. Thermal behavioral differences between the RCNs and the original cellulose sources may be due to different decomposition–gasification

Table 3
Onset degradation temperature (T_0), maximum thermal degradation temperature (T_{max}), maximum weight loss rate (R_{max}), and char yield (CY) at 550 °C in the thermal degradation process of each sample obtained from TG and DTG curves.

Sample	T_0 (°C)	T_0 (°C)		Stagel		Stage II
		T_{max} (°C)	R_{max} (%/°C)	T_{max} (°C)	R_{max} (%/°C)	CY (wt%)
MCC	300.3	–	–	344.3	2.4	1.9
MRC II	205.8	254.7	0.4	328.4	0.9	6.7
Cotton	310.6	–	–	340.3	2.7	7.9
CRC II	200.8	258.7	0.4	325.8	0.9	10.3

processes. T_0 and T_{max} values of M-RCNs and C-RCNs were lower than the representative values for original MCC and cotton. Similar phenomenon was reported previously (Chen, Wang, & Liu, 2012). This demonstrated that the thermal stability of cellulose decreased after regeneration from $[BMIM]^+[Cl]^-$, which was consistent with the observed decrease of CI of cellulose dissolved in $[BMIM]^+[Cl]^-$. Although the regenerated cellulose had a lower onset temperature for decomposition, the char yield (CY) at 550 °C of M-RCNs and C-RCNs was greater than that of MCC or cotton (Table 3). The decrease in thermal stability could be due to several reasons. First, the adhesion of the anion group from the ionic liquid onto the surface of cellulose nanoparticles could have an effect on thermal behavior of cellulose (Kim, Nishiyama, Wada, & Kuga, 2001). Second, the high surface area of cellulose nanoparticles might diminish their thermostability due to the increased exposure surface area to heat (Lu & Hsieh, 2010).

3.5. Mechanism of the dissolution and regeneration of cellulose in $[BMIM]^+[Cl]^-$

Based on the results obtained above, the possible mechanism of dissolution of cellulose in $[BMIM]^+[Cl]^-$ could be inferred as follows. Native cellulose is a semi-crystalline polymer consisting of highly crystalline and amorphous regions. The inter- and intra-molecular hydrogen bonds of cellulose chains need to be disrupted in order to dissolve cellulose (Jin et al., 2012). The previous studies on the mechanism of the cellulose dissolution in ILs showed that the interactions between the hydroxyls of cellulose and the anions of the ILs played an important role in this process. When cellulose was dissolved in $[BMIM]^+[Cl]^-$, the ion pairs in $[BMIM]^+[Cl]^-$ dissociated to individual $[BMIM]^+$ cation and $[Cl]^-$ anion (Jin et al., 2012). The hydrogen and oxygen atoms of the cellulose molecules formed electron donor-electron acceptor complexes with the charged species of the $[BMIM]^+[Cl]^-$ (Pinkert, Marsh, Pang, & Staiger, 2009). On one hand, the dissociated $[BMIM]^+[Cl]^-$ enters the space between the cellulose chains. Then free $[Cl]^-$ anions associated with the hydroxyl proton of H—O···H bonds, and meanwhile, free $[BMIM]^+$ cations attack the oxygen atoms of H—O···H bonds. This interaction resulted in the separation of the hydroxyl groups of the different cellulose chains leading to the swelling behavior of cellulose fibrils. On the other hand, within a single cellulose chain, $[Cl]^-$ anions attack the carbon atoms of the β-1,4-glycosidic bonds and $[BMIM]^+$ with its electron rich aromatic π system interacted with the oxygen atom of the β-1,4-glycosidic bonds via nonbonding or π electrons. These interactions resulted in the breakage of the extensive hydrogen bonding network between two cellulose chains and the breakage of the β-1,4-glycosidic bonds within cellulose chains, which further led to the dissolution and degradation of cellulose into a molecular level (Kosan, Michels, & Meister, 2008). It was also reported that $[Cl]^-$ anions were mainly responsible for the effective dissolution of cellulose due to the higher strength and larger interaction energy of $[Cl]^-$ anions with the oligomer.

However, the subtle structural and size changes of cellulose occurred not only in the solubilization state but also in the reconstitution stage. Rapid mixing of the cellulose/$[BMIM]^+[Cl]^-$ solution with distilled water (polar solvent) resulted in precipitation of cellulose as powdery flocs. This phenomenon indicated that the cellulose dissolved in $[BMIM]^+[Cl]^-$ could reconstitute with the presence of anti-solvent. In the regeneration process, hydrogen-bonding properties still played a key role in the reconstruction of cellulose in cellulose/water/$[BMIM]^+[Cl]^-$ system (Swatloski et al., 2002). Because the O—H···O type H-bond is far stronger than the C—H···O type H-bond, $[BMIM]^+[Cl]^-$ prefers to form H-bonds with water molecules (Ding et al., 2012). This is the reason why $[BMIM]^+[Cl]^-$ has a strong water absorbability. As a result, the H-bonds between cellulose and $[BMIM]^+[Cl]^-$ were weakened with addition of water into cellulose/$[BMIM]^+[Cl]^-$ system. During the regeneration process, the H-bonds between cellulose chains reconnected with each other, resulting in the reconstitution and precipitation of cellulose. However, the TGA data showed that the onset decomposition temperature for regenerated cellulose was about 100 °C lower than that for original cellulose. This decreased thermal stability indicated the decrease in molecular weight of regenerated cellulose (Chen et al., 2012). In addition, WXRD results suggested that the crystallinity index of cellulose decreased for both MCC and cotton during dissolution and regeneration. The lower crystallinity of regenerated cellulose indicated that this interaction was not sufficient to completely reestablish the strong H-bond network of original microcrystalline cellulose. Therefore, the cellulose dissolved in $[BMIM]^+[Cl]^-$ could only regain a lower crystallinity and reconstitute into nano-sized particles with cellulose II crystalline allomorph upon the addition of water during regeneration. The nanoparticles could be further dispersed steadily in water through high-pressure homogenization treatment. Based on the initial weight of the cellulose in $[BMIM]^+[Cl]^-$, the yield of the reconstituted cellulose II nanoparticles was estimated to be 30–40 wt.%, supporting the aforementioned hypothesis on the formation of regenerated cellulose nanoparticles. The theoretical interpretations provided assistance to develop appropriate IL-based solvents for dissolution and processing of cellulose (Xu, Pan, Wang, Zhang, & Liu, 2012).

4. Conclusions

In this work, regenerated cellulose II nanoparticles were successfully produced from MCC and cotton by using a combined IL and high-pressure homogenization treatment. The crystal structures of cellulose were transformed from cellulose I to II with decreased crystallinities during the ILs treatment. The fiber-type C-RCNs had an average length of 123 ± 34 nm, an average width of 12 ± 5 nm, while the fiber-type M-RCNs had an average length of 112 ± 42 nm, an average width of 12 ± 3 nm. The original samples showed similar one-step pyrolysis processes, while the M-RCNs and C-RCNs had similar two-step pyrolysis processes. The dimension distribution of cellulose II nanoparticles regenerated from $[BMIM]^+[Cl]^-$ followed the asymmetrical log-normal distribution. The properties of RCNs characterized in this study provided some fundamental information for the potential application of RCNs in biomedicine field such as tablet excipients.

Acknowledgments

The authors are thankful for the financial support from Louisiana Board of Regents [LEQSF-EPS(2013)-PFUND-318], USDA NIFA (Award No. 2008-38814-04771), Chinese Scholarship Council (CSC No.: 2009660015), and the National Natural Science Foundation of China (Grant no. 31070505).

References

Azubuike, C. P., Rodriguez, H., Okhamafe, A. O., & Rogers, R. D. (2012). Physicochemical properties of maize cob cellulose powders reconstituted from ionic liquid solution. *Cellulose*, *19*(2), 425–433.

Chen, H.-Z., Wang, N., & Liu, L.-Y. (2012). Regenerated cellulose membrane prepared with ionic liquid 1-butyl-3-methylimidazolium chloride as solvent using wheat straw. *Journal of Chemical Technology & Biotechnology*, *87*, 1634–1640.

Ding, Z. D., Chi, Z., Gu, W. X., Gu, S. M., Liu, J. H., & Wang, H. J. (2012). Theoretical and experimental investigation on dissolution and regeneration of cellulose in ionic liquid. *Carbohydrate Polymers*, *89*(1), 7–16.

Elazzouzi-Hafraoui, S., Nishiyama, Y., Putaux, J. L., Heux, L., Dubreuil, F., & Rochas, C. (2008). The shape and size distribution of crystalline nanoparticles prepared by acid hydrolysis of native cellulose. *Biomacromolecules*, *9*(1), 57–65.

Gao, Q., Shen, X., & Lu, X. (2011). Regenerated bacterial cellulose fibers prepared by the NMMO•H_2O process. *Carbohydrate Polymers*, *83*(3), 1253–1256.

Gutowski, K. E., Broker, G. A., Willauer, H. D., Huddleston, J. G., Swatloski, R. P., Holbrey, J. D., et al. (2003). Controlling the aqueous miscibility of ionic liquids: aqueous biphasic systems of water-miscible ionic liquids and water-structuring salts for recycle, metathesis, and separations. *Journal of the American Chemical Society*, *125*(22), 6632–6633.

Hirota, M., Tamura, N., Saito, T., & Isogai, A. (2012). Cellulose II nanoelements prepared from fully mercerized, partially mercerized and regenerated celluloses by 4-acetamido-TEMPO/NaClO/$NaClO_2$ oxidation. *Cellulose*, *19*(2), 435–442.

Jiang, G. S., Huang, W. F., Li, L., Wang, X., Pang, F. J., Zhang, Y. M., et al. (2012). Structure and properties of regenerated cellulose fibers from different technology processes. *Carbohydrate Polymers*, *87*(3), 2012–2018.

Jin, Z. W., Wang, S., Wang, J. Q., & Zhao, M. X. (2012). Effects of plasticization conditions on the structures and properties of cellulose packaging films from ionic liquid [BMIM]Cl. *Journal of Applied Polymer Science*, *125*(1), 704–709.

Kim, D. Y., Nishiyama, Y., Wada, M., & Kuga, S. (2001). High-yield carbonization of cellulose by sulfuric acid impregnation. *Cellulose*, *8*(1), 29–33.

Kosan, B., Michels, C., & Meister, F. (2008). Dissolution and forming of cellulose with ionic liquids. *Cellulose*, *15*(1), 59–66.

Kumar, R., Mago, G., Balan, V., & Wyman, C. E. (2009). Physical and chemical characterizations of corn stover and poplar solids resulting from leading pretreatment technologies. *Bioresource Technology*, *100*(17), 3948–3962.

Kumar, V., de la Luz Reus-Medina, M., & Yang, D. (2002). Preparation, characterization, and tabletting properties of a new cellulose-based pharmaceutical aid. *International Journal of Pharmaceutics*, *248*(1–2), 261.

Kuo, C. H., & Lee, C. K. (2009). Enhancement of enzymatic saccharification of cellulose by cellulose dissolution pretreatments. *Carbohydrate Polymers*, *77*(1), 41–46.

Lan, W., Liu, C. F., Yue, F. X., Sun, R. C., & Kennedy, J. F. (2011). Ultrasound-assisted dissolution of cellulose in ionic liquid. *Carbohydrate Polymers*, *86*(2), 672–677.

Lee, S. H., Doherty, T. V., Linhardt, R. J., & Dordick, J. S. (2009). Ionic liquid-mediated selective extraction of lignin from wood leading to enhanced enzymatic cellulose hydrolysis. *Biotechnology and Bioengineering*, *102*(5), 1368–1376.

Li, C. L., Knierim, B., Manisseri, C., Arora, R., Scheller, H. V., Auer, M., et al. (2010). Comparison of dilute acid and ionic liquid pretreatment of switchgrass: biomass recalcitrance, delignification and enzymatic saccharification. *Bioresource Technology*, *101*(13), 4900–4906.

Li, Q., He, Y. C., Xian, M., Jun, G., Xu, X., Yang, J. M., et al. (2009). Improving enzymatic hydrolysis of wheat straw using ionic liquid 1-ethyl-3-methyl imidazolium diethyl phosphate pretreatment. *Bioresource Technology*, *100*(14), 3570–3575.

Liu, H. Y., Liu, D. G., Yao, F., & Wu, Q. L. (2010). Fabrication and properties of transparent polymethylmethacrylate/cellulose nanocrystals composites. *Bioresource Technology*, *101*(14), 5685–5692.

Lu, P., & Hsieh, Y. L. (2010). Preparation and properties of cellulose nanocrystals: Rods, spheres, and network. *Carbohydrate Polymers*, *82*(2), 329–336.

Mahmoudian, S., Wahit, M. U., Ismail, A. F., & Yussuf, A. A. (2012). Preparation of regenerated cellulose/montmorillonite nanocomposite films via ionic liquids. *Carbohydrate Polymers*, *88*(4), 1251–1257.

Mansikkamäki, P., Lahtinen, M., & Rissanen, K. (2007). The conversion from cellulose I to cellulose II in NaOH mercerization performed in alcohol–water systems: an X-ray powder diffraction study. *Carbohydrate Polymers*, *68*(1), 35–43.

Marchessault, R. H., Morehead, F. F., & Walter, N. M. (1959). Liquid crystal systems from fibrillar polysaccharides. *Nature*, *184*(4686), 632–633.

Pinkert, A., Marsh, K. N., Pang, S. S., & Staiger, M. P. (2009). Ionic liquids and their interaction with cellulose. *Chemical Reviews*, *109*(12), 6712–6728.

Quan, S.-L., Kang, S.-G., & Chin, I.-J. (2010). Characterization of cellulose fibers electrospun using ionic liquid. *Cellulose*, *17*(2), 223–230.

Ray, D., & Sarkar, B. K. (2001). Characterization of alkali-treated jute fibers for physical and mechanical properties. *Journal of Applied Polymer Science*, *80*(7), 1013–1020.

Shibazaki, H., Kuga, S., & Okano, T. (1997). Mercerization and acid hydrolysis of bacterial cellulose. *Cellulose*, *4*(2), 75–87.

Swatloski, R. P., Spear, S. K., Holbrey, J. D., & Rogers, R. D. (2002). Dissolution of cellose with ionic liquids. *Journal of the American Chemical Society*, *124*(18), 4974–4975.

Tamai, N., Tatsumi, D., & Matsumoto, T. (2004). Rheological properties and molecular structure of tunicate cellulose in LiCl/1,3-dimethyl-2-imidazolidinone. *Biomacromolecules*, *5*(2), 422–432.

Wang, L. L., Han, G. T., & Zhang, Y. M. (2007). Comparative study of composition, structure and properties of *Apocynum venetum* fibers under different pretreatments. *Carbohydrate Polymers*, *69*(2), 391–397.

Wang, N., Ding, E., & Cheng, R. S. (2008). Preparation and liquid crystalline properties of spherical cellulose nanocrystals. *Langmuir*, *24*(1), 5–8.

Wang, N., Ding, E. Y., & Cheng, R. S. (2007). Thermal degradation behaviors of spherical cellulose nanocrystals with sulfate groups. *Polymer*, *48*(12), 3486–3493.

Xu, H., Pan, W. X., Wang, R. X., Zhang, D. J., & Liu, C. B. (2012). Understanding the mechanism of cellulose dissolution in 1-butyl-3-methylimidazolium chloride ionic liquid via quantum chemistry calculations and molecular dynamics simulations. *Journal of Computer-Aided Molecular Design*, *26*(3), 329–337.

Yue, Y. Y., Zhou, C. J., French, A. D., Xia, G., Han, G. P., Wang, Q. W., et al. (2012). Comparative properties of cellulose nano-crystals from native and mercerized cotton fibers. *Cellulose*, *19*(4), 1173–1187.

Zhang, H., Wang, Z. G., Zhang, Z. N., Wu, J., Zhang, J., & He, H. S. (2007). Regenerated-cellulose/multiwalled-carbon-nanotube composite fibers with enhanced mechanical properties prepared with the ionic liquid 1-allyl-3-methylimidazolium chloride. *Advanced Materials*, *19*(5), 698–704.

Zhang, X. M., Liu, X. Q., Zheng, W. G., & Zhu, J. (2012). Regenerated cellulose/graphene nanocomposite films prepared in DMAC/LiCl solution. *Carbohydrate Polymers*, *88*(1), 26–30.

Zhao, H. B., Kwak, J. H., Wang, Y., Franz, J. A., White, J. M., & Holladay, J. E. (2007). Interactions between cellulose and N-methylmorpholine-N-oxide. *Carbohydrate Polymers*, *67*(1), 97–103.

Zhu, S. D., Wu, Y. X., Chen, Q. M., Yu, Z. N., Wang, C. W., Jin, S. W., et al. (2006). Dissolution of cellulose with ionic liquids and its application: A mini-review. *Green Chemistry*, *8*(4), 325–327.